Declarations of interest: none.

# Impact of non-symmetric confinement on the flame dynamics of a lean-premixed swirl flame

S. Herff<sup>a,\*</sup>, K. Pausch<sup>b</sup>, S. Loosen<sup>a</sup>, W. Schröder<sup>a,c</sup>

#### Abstract

The impact of confinement on a turbulent lean premixed swirl flame is investigated using a finite-volume large-eddy simulation method to solve the compressible Navier-Stokes equations and a combined G-equation progress variable approach to model the flame. The geometry is an experimentally investigated burner by Moeck et al. [Combust. Flame, 159, 2650-2668 (2012)] in which a precessing vortex core (PVC) and a self-excited thermoacoustic instability occur. To analyze the effect of confinement on the M-shaped flame, three configurations are investigated, i.e., an unconfined configuration, a symmetric confined configuration, and a non-symmetric confined configuration. The symmetric confined configuration corresponds to the experimental burner and the numerical results are in good agreement with the measurements. The flow fields of the confined and unconfined configurations differ significantly due to a more pronounced PVC downstream of the injection

Email address: s.herff@aia.rwth-aachen.de (S. Herff)

<sup>&</sup>lt;sup>a</sup>Institute of Aerodynamics RWTH Aachen University, Wüllnerstraße 5a, Aachen 52062, Germany

<sup>&</sup>lt;sup>b</sup> Jülich Supercomputing Centre, Forschungszentrum Jülich GmbH, Wilhelm-Johnen-Str., Jülich 52425, Germany

<sup>&</sup>lt;sup>c</sup>JARA Center for Simulation and Data Science, RWTH Aachen University, Seffenter Weg 23, Aachen 52074, Germany

<sup>\*</sup>Corresponding author:

tube in the confined configurations. The numerical results confirm experimental findings from the literature, i.e., the confinement defines the recirculation zones and the turbulence intensity of the swirling jets. Furthermore, the present results show that the limit-cycle amplitude of the thermoacoustic instability, which occurs in the confined configurations due to a resonant coupling of the flame with the acoustic quarter-wave mode of the combustion chamber, is significantly reduced in the non-symmetric confined configuration. The mode determined by a dynamic mode analysis (DMD) that describes the impact of the acoustic quarter-wave mode on the velocity field only occurs in the symmetric confined configuration. Consequently, a lower coupling of the acoustic oscillations due to the thermoacoustic instability with the flame is evident. The results emphasize the sensitivity of the thermoacoustic instabilities on the confinement configuration and indicate the dependence of their oscillation amplitudes on the location of the swirl flame in the combustion chamber.

Keywords: Swirl Flame, Large-Eddy Simulation, Precessing Vortex Core, Thermoacoustic Instability

#### 1. Introduction

Turbulent lean premixed swirl flames are of interest in industrial applications, e.g., gas turbines. Lean premixing reduces pollutant emissions and the swirling flow causes a recirculation zone on the centerline of the flame which leads to a stable and compact flame with relatively high rate of fuel burning. Combustion instabilities may occur due to a resonant coupling of the acoustic sources of the flame with the acoustic modes of the combustion

chamber. Such combustion instabilities must be prevented since they can damage the burner assembly [1]. Furthermore, due to the swirling flow a helical flow instability, i.e., a precessing vortex core (PVC), is often observed in the combustion chamber.

Since combustion instabilities and PVC are frequently observed simultaneously in swirling flames their interaction has been investigated experimentally and numerically in numerous studies. Kim et al. [2] investigated an interference mechanism of acoustic and convective disturbances. They showed that the flame transfer function (FTF), which is the response of the flame to acoustic disturbances, is a function of the swirler position due to the interaction with vorticity waves which are induced when acoustic waves pass through the swirler geometry. They found that in phase interference of acoustic and vorticity waves leads to high amplitude limit-cycle oscillations. Caux-Brisebois et al. [3] investigated high amplitude thermoacoustic velocity coupling of a burner, which evidences a precessing vortex core (PVC). They used a doubly-phase-resolved analysis resolving their measurement data with respect to the phase in the acoustic cycle and the azimuthal position of the PVC relative to the measurement plane. Repeatable oscillatory flow-flame interactions were observed at each azimuthal position of the PVC over the thermoacoustic cycle. Furthermore, a deformation of the PVC at the acoustic frequency was caused by the changing pressure difference between the plenum and the combustion chamber. Moeck et al. [4] used a generic experimental burner to study the non-linear interaction between acoustic oscillations and the PVC. The flame shape varied between V- and M-shape and self-excited instabilities were observed for various operating conditions. They showed

that the interaction of the PVC with the acoustic instability frequency can lead to an interaction mode at the frequency being the difference of the PVC and the acoustic frequencies. Significant disturbances of the flame by flow structures in the outer shear layer were observed and Moeck et al. concluded that the confinement has a considerable impact on the dynamics of the flame that is associated with the PVC.

In general, swirl flames in practical systems are confined by a combustion chamber. However, as discussed in a review about confined and unconfined laboratory-scaled swirl burners by Al-abdeli et al. [5] there are still open questions regarding the effects of confinement on the flow field and the flame dynamics. Confined and unconfined swirl flames were numerically investigated and compared to experimental results by Nogenmyr et al. [6]. They showed that the confinement has a significant impact on the flow field by enlarging the central recirculation zone. The outer recirculation zone was only present in the confined case. However, the flow field shortly downstream of the injector was hardly affected by the confinement. Similar results were reported by Khalilhasan et al. [7]. The confinement increased the strength of the inner and outer recirculation zones and the turbulent kinetic energy (TKE) increased in the confined configuration. De Rosa et al. [8] studied the flame-wall interaction of swirl flames experimentally by varying the confinement ratio and Tay Wo Chong et al. [9] performed large-eddy simulations (LES) for varying confinement ratios and wall boundary condition formulations. Both studies showed that the FTF was influenced by the confinement ratio and the FTF could not be generalized since the behavior of the flame and the flow field changed significantly for the various confinements. Wang et al. [10] experimentally investigated acoustically excited unconfined and confined swirl flames. They used a confinement ratio for the confined configurations which resulted in small discrepancies between the flow fields of the unconfined and confined configurations. However, they found that the flame dynamics and heat release fluctuations are still affected by the confinement.

The results of these studies show that the details of the confinement have a significant impact on the dynamics of swirl flames. However, the confinement was symmetric, effects of non-symmetric confinement were not investigated. Kim et al. [11] demonstrated that symmetry breaking of the flow field can strongly affect combustion instabilities. However, their study focused on non-symmetry due to multi-flame configurations. Note that the effect of non-symmetry due to multiple flames can be significantly different from the effect of non-symmetric confinement. Further studies are necessary to understand the effects of confinement on the dynamics of the flame. To the best of the authors' knowledge, the effect of non-symmetric confinement on single swirl flames was not yet investigated in the journal literature.

In the current study, the effect of confinement on the flow field and the dynamics of a single swirl flame are numerically investigated by considering three configurations. An M-shaped flame is analyzed in an unconfined configuration, a symmetric confined configuration, and a non-symmetric confined configuration. Highly resolved LES are used to ensure a high quality of the computed flow field and the acoustic sources such that the impact of confinement on the thermoacoustic instability can be analyzed.

A grid convergence study for the symmetric confined configuration was performed in [12] and it was shown that the crucial turbulent scales are resolved. Due to the high quality of the computations a detailed analysis of the acoustic emission of the unconfined and the symmetric confined flames could be performed in Pausch et al. [13]. The design of the burner by Moeck et al. [4] is used such that the results of the symmetric confined configuration can be validated by experimental results.

By comparatively juxtaposing the results of the three configurations the following questions are answered in this study. What is the effect of confinement on the recirculation zones, the PVC, the dynamics of the flame, and the distribution of the turbulence intensity in the swirling jet? How does non-symmetric confinement influence the limit-cycle amplitude of the thermoacoustic instability? The dynamic modes of the flow field data are analyzed using a dynamic mode decomposition (DMD) algorithm. That is, dynamic modes are detected which describe the PVC and the impact of the thermoacoustic instability on the velocity field. The corresponding modes are temporally reconstructed and analyzed.

The study is structured as follows. First, the numerical methods are introduced. Then, the burner geometry and the numerical configurations are briefly discussed for consistency. The validation of the numerical results from Herff et al. [12] is briefly reviewed before the results of the three investigated configurations are analyzed. Finally, conclusions are drawn.

#### 2. Numerical Methods

In the following, the conservative finite-volume method for the solution of the Navier-Stokes equations coupled with a level-set solver for the G-equation introduced in [14, 15], which are features of the in-house developed software

m-AIA (multiphysics Aerodynamisches Institut Aachen), and the dynamic mode decomposition (DMD) algorithm are presented.

## 2.1. Flow field and combustion field

The three-dimensional unsteady compressible Navier-Stokes equations are solved using the combined G-equation progress variable modeling approach by Moureau et al. [16] to compute the turbulent lean premixed swirl flame.

The governing equations read

$$\frac{\partial \mathbf{Q}}{\partial t} + \nabla \cdot \mathbf{H} = \dot{\mathbf{W}}, \qquad (1)$$

where  $\nabla = \left[\frac{\partial}{\partial x}, \frac{\partial}{\partial y}, \frac{\partial}{\partial z}\right]^T$  is the vector of spatial derivatives in the Cartesian coordinate system. The vector of conservative variables  $\boldsymbol{Q}$  and the flux vector  $\boldsymbol{H}$ , which is decomposed into an inviscid  $\boldsymbol{H}^i$  and a viscous part  $\boldsymbol{H}^v$ , read in Favre-filtered non-dimensional form

$$Q = \begin{pmatrix} \bar{\rho} \\ \bar{\rho}\tilde{\mathbf{v}} \\ \bar{\rho}\tilde{E} \\ \bar{\rho}\tilde{c} \end{pmatrix}, \qquad H = H^{i} - H^{v} = \begin{pmatrix} \bar{\rho}\tilde{\mathbf{v}} \\ \bar{\rho}\tilde{\mathbf{v}}\tilde{\mathbf{v}} + \bar{p}\underline{\mathbf{I}} \\ \tilde{\mathbf{v}}\left(\bar{\rho}\tilde{E} + \bar{p}\right) \\ \bar{\rho}\tilde{\mathbf{v}}\tilde{c} \end{pmatrix} + \frac{1}{Re_{0}} \begin{pmatrix} 0 \\ \frac{\tilde{\tau}}{2} + \underline{\tau_{sgs}} \\ \frac{\tilde{\tau}}{2}\tilde{\mathbf{v}} + \tilde{\mathbf{q}} + \Gamma_{sgs} \\ \mathbf{J}_{c} \end{pmatrix},$$

$$(2)$$

where  $\underline{I}$  is the unit matrix,  $\rho$  denotes the density,  $\boldsymbol{v}$  the velocity vector, E the total specific energy, c the progress variable, p the pressure,  $\underline{\boldsymbol{\tau}}$  the stress tensor,  $\boldsymbol{q}$  the vector of heat conduction, and  $\boldsymbol{J}_c$  the diffusive flux of the progress variable. The Reynolds number  $Re_0 = \frac{\rho_0 a_0 l}{\mu_0}$  is based on the speed of sound  $a_0$  at stagnation values denoted by the subscript 0 and the characteristic length l. The following quantities are used for the non-dimensionalization of the variables:  $\rho_0 a_0^2$  for the pressure,  $a_0$  for the velocity,  $\rho_0$  for the density, and

 $\frac{l}{a_0}$  for the time. The subgrid-scale stress tensor  $\underline{\tau_{sgs}}$  and the subgrid-scale energy  $\Gamma_{sgs}$  require a model which is explained later. For further details on the subgrid-scale terms the reader is referred to, e.g., Meinke et al. [17]. The dynamic viscosity  $\mu$  is determined by Sutherland's law. Assuming a Newtonian fluid and a zero bulk viscosity, the stress tensor  $\underline{\tau}$  is formulated as

$$\underline{\tilde{\tau}} = -\mu \left( \nabla \tilde{\boldsymbol{v}} + (\nabla \tilde{\boldsymbol{v}})^T - \frac{2}{3} (\nabla \cdot \tilde{\boldsymbol{v}}) \underline{\boldsymbol{I}} \right). \tag{3}$$

The heat conduction  $\boldsymbol{q}$  is determined by Fourier's law  $\boldsymbol{q} = -\frac{\lambda}{Pr(\gamma-1)}\nabla \tilde{T}$ , where T is the temperature,  $\gamma$  denotes the ratio of specific heats which is assumed to be constant, and the Prandtl number  $Pr = \frac{\mu_0 c_{p,0}}{\lambda_0}$  with the specific heat at constant pressure  $c_{p,0}$ . Assuming a constant Prandtl number the thermal conductivity can be computed as  $\lambda\left(\tilde{T}\right) = \mu\left(\tilde{T}\right)$ . The diffusive flux of the progress variable c is determined by

$$\boldsymbol{J}_c = \frac{1}{Pr} \rho_{\infty}^u D \nabla \tilde{c},\tag{4}$$

where  $\rho_{\infty}^u$  denotes the density of the unburnt gas in the freestream and the diffusivity D is assumed to be constant and is evaluated in the unburnt gas. The source term  $\dot{\boldsymbol{W}}$  reads

$$\dot{\mathbf{W}} = (0, \mathbf{0}, \mathcal{Q}\dot{\bar{\omega}}_c, \dot{\bar{\omega}}_c)^T , \qquad (5)$$

where  $\mathcal{Q}$  denotes the heat of the chemical reaction. The chemical reaction rate  $\dot{\bar{\omega}}_c$  is determined by

$$\bar{\dot{\omega}}_c = Re \, Pr \, \bar{\rho} \frac{\rho_{\infty}^u}{\rho_{\infty}^b} \, R_r \, (1 - c) \, \Psi \left( \check{G}(\boldsymbol{x}, t), \sigma \right) \,, \tag{6}$$

where the quantity  $\rho_{\infty}^{b}$  is the density of the burnt gas in the freestream. The

Ferziger and Echeckki model constant  $R_r$  reads

$$R_r = \frac{1}{1 - c^0} \left( \frac{1}{1 - c^0} - 1 \right) \frac{\left(s^u\right)^2}{D},\tag{7}$$

where  $c^0$  is the reduced inner layer temperature and  $s^u$  is the local curvature-corrected flame speed evaluated with respect to the unburnt gas. The function  $\Psi\left(\check{G}\left(\boldsymbol{x},t\right),\sigma\right)$  in equation 6 defines the reaction rate profile and can be artificially thickened by the parameter  $\sigma$ . The value of sigma with respect to the cell spacing  $\Delta$  is  $\frac{\sigma}{\Delta}=1$  in the computations within this paper. It has been shown in [18] that the effect of flame thickening on the sound emission of lean premixed flames is negligible for  $\frac{\sigma}{\Delta}<4$ . The reaction rate profile depends on the distance to the flame front denoted by G.

The evolution of the G-field is defined by the G-equation [19, 20]

$$\frac{\partial \check{G}}{\partial t} + \left(\tilde{\boldsymbol{v}} + \frac{\rho_{\infty}^{u}}{\bar{\rho}} \hat{\tilde{\boldsymbol{s}}}_{t,u} \check{\boldsymbol{n}}\right) \cdot \nabla \check{G} = 0, \tag{8}$$

where

$$\check{\boldsymbol{n}} = -\frac{1}{|\nabla \check{G}|} \left( \partial \check{G} / \partial x, \ \partial \check{G} / \partial y, \ \partial \check{G} / \partial z \right)^{T} . \tag{9}$$

For an arbitrary variable  $\Theta$ , the notation  $\check{\boldsymbol{x}}_f$  indicates a variable defined at the filtered flame front location  $\hat{\boldsymbol{x}}_f$  such that  $\check{\boldsymbol{G}}(\boldsymbol{x},t) = G_0$ , the notation  $\hat{\Theta}$  represents variables, which are filtered by the surface integral over the resolved flame front,  $\check{\Theta}$  represents Favre filtered, and  $\Theta$  spatially filtered variables. In equation 8, the quantity  $\check{\boldsymbol{v}}$  is the local Favre filtered flow velocity,  $\rho_{\infty}^u$  the freestream density in the unburnt gas,  $\bar{\rho}$  is the spatially filtered density

$$\bar{\rho} = \frac{\rho_{\infty}^u}{1 - c\left(\rho_{\infty}^b - \rho_{\infty}^u\right)/\rho_{\infty}^b} \quad , \tag{10}$$

and  $\check{\boldsymbol{n}}$  the normal vector at  $\hat{\boldsymbol{x}}_f$  pointing towards the unburnt fuel-air mixture. The zero-value level-set contour  $G=G_0=0$  describes the motion of the inner-layer temperature contour of the flame and the scalar G is defined to be positive in the burnt gas and negative in the unburnt gas. The flame speed is modeled by

$$\hat{\tilde{s}}_{t,u} = \hat{\tilde{s}}_{l,0} (1 - \kappa l_c) + s_T, \tag{11}$$

where the laminar flame speed  $\hat{\hat{s}}_{l,0}$  is corrected by the curvature  $\check{\kappa} = \nabla \cdot \boldsymbol{n}$  multiplied by the Markstein length  $l_c$  and the term

$$s_T = s_t - D_{t,k}\check{\kappa} \tag{12}$$

models the flame-flow interaction on the subgrid level [20]. The turbulent diffusivity  $D_{t,k}$  is evaluated depending on the filtered Damköhler number  $Da_{\Delta}$ . That is, if  $Da_{\Delta} < 1$ 

$$D_{t,k} = D_t \tag{13}$$

and otherwise

$$D_{t,k} = D_t D a_{\Delta}^{-2}. \tag{14}$$

The turbulent flame speed on the subgrid  $s_t = \hat{\tilde{s}}_{l,0} \left( A + \sqrt{B} \right)$  accounts for wrinkling effects on the subgrid on the flame speed. The model constants A and B are

$$A = -\frac{b_2^2 \nu_t \hat{\hat{s}}_{l,0}}{2b_1 S c_t D u_{\Lambda}'},\tag{15}$$

$$B = A^2 + \frac{b_2^2 \nu_t}{Sc_t D},\tag{16}$$

with the constants  $b_1 = 2.0$  and  $b_2 = 1.0$ , the turbulent viscosity  $\nu_t$ , the turbulent Schmidt number  $Sc_t = 0.4$ , the diffusivity D, and the subfilter

velocity  $u'_{\Delta}$ . The subfilter velocity is estimated by  $u'_{\Delta} = \frac{\nu_t}{\Delta x}$ , where  $\Delta x$  is the cell spacing. Note that this is a rough estimation of  $u'_{\Delta}$  which is likely to deviate from the exact subfilter velocity. A more accurate estimation could be achieved by considering an additional transport equation for the subgrid turbulent kinetic energy as shown in Schumann [21], which is then used to approximate  $u'_{\Delta}$ . However, this approach is computationally expensive due to the additional equation. An alternative estimation of  $u'_{\Delta}$  from the resolved velocity field, which excludes the dilatational part of the velocity field, was proposed by Colin et al. [22]. Due to the high resolution of the investigated configurations in this study  $s_t$  is small. Thus, it is expected that the turbulent flame speed on the subgrid has a negligible effect on the qualitative results. Note that hydrodynamic strain effects on the flame speed are neglected by the combustion model which limits the model to moderate flame stretch without local flame extinction on the flame surface. The combustion model is valid in the thin reaction zone and the corrugated flamelet regime |20|. This combustion modeling approach has been used extensively and the results showed a high accuracy of the dynamics of the flame surface for several canonical problems, e.g., flame-vortex interaction [15, 16], Darrieus-Landau instability [23], and an accurate prediction of the mean heat release rate distribution and the mean turbulent mass consumption speed [19]. Furthermore, this approach has been recently used to analyze the noise sources of lean-premixed flames [13, 24].

To model the subgrid turbulence the large-eddy simulation (LES) is based on the monotone integrated LES (MILES) approach [25]. The MILES approach requires a relatively high resolution. However, for an appropriate

resolution this subgrid formulation yields accurate results independent of the investigated setup<sup>1</sup>. The state variables on the cell surfaces are computed by a second-order accurate monotone upstream-centered scheme for conservation laws (MUSCL) and the surface fluxes are determined using an upwind-biased scheme. The viscous terms are discretized by second-order accurate central differences, while the convective terms are approximated by a second-order accurate modified low-dissipation advection upstream splitting method (AUSM) scheme. The time integration is performed using a third-order total-variation diminishing (TVD) Runge-Kutta scheme [26]. To resolve the wall boundaries, a strictly conservative cut-cell approach is used. Small cut cells are treated using a flux-redistribution method [27]. Conservativeness at wall-mesh variations is maintained using the approach discussed in [28].

The motion of the flame front is described by the zero level-set contour of the G-equation. Details on the G-equation, the combustion model, and the modeling of the flame speed are presented in Pitsch [20]. The G-equation is solved by a fifth-order upwind-central scheme [29] for the spatial discretization and the aforementioned third-order TVD Runge-Kutta scheme [26]. A high-order constrained reinitialization scheme HCR-2 [14] is used to reini-

<sup>&</sup>lt;sup>1</sup>Note that a grid convergence study was performed in Herff et al. [12] for the symmetric confined swirl burner setup which is analyzed in this study to ensure that the root-mean square profiles of the velocity components are converged. Since the quality of the applied subgrid turbulence model is independent from the geometric details of the numerical setup, it is expected that the qualitative results of the non-symmetric confined configuration have a high accuracy.

tialize the signed-distance property. The computational cost of the level-set solver is minimized by solving the G-equation only in a narrow band near the flame front and adapting the level-set grid according to the flame location. This combustion modeling approach has been shown to satisfactorily capture the dynamics of the flame surface for several canonical problems, e.g., flame-vortex interaction [15, 16], Darrieus-Landau instability [23], and to accurately predict the mean heat release rate distribution and the mean turbulent mass consumption speed [19]. Furthermore, this approach has been used to accurately compute the interaction of acoustic modes with an unconfined turbulent jet flame [30] and to analyze the noise sources of lean-premixed flames [13].

Note that the present computations use a static mesh for the finite-volume solver and a solution adaptive mesh for the level-set solver. The finite-volume solver and the level-set solver are coupled using a joint hierarchical mesh. A fully automated dynamic load balancing method was adapted for the coupled finite-volume and level-set solvers. For details on the solver coupling and the dynamic load balancing method the reader is referred to [12].

#### 2.2. Dynamic Mode Decomposition

The DMD algorithm, which is based on Schmid [31], requires a data matrix  $\Omega = [\Omega_0, \Omega_1, ..., \Omega_N]$  which consists of a sequence of equidistantly sampled snapshots where  $\Omega_n = \Omega(x, y, z, t_n)$  represents the data field at the time  $t_n$ . The data matrix is projected by the DMD onto a set of non-orthogonal spatial modes

$$\underbrace{\left[\Omega_{0}, \Omega_{1}, ..., \Omega_{N-1}\right]}_{\Omega} \approx \underbrace{\left[\Phi_{0}, \Phi_{1}, ..., \Phi_{N}\right]}_{\Phi} \cdot \mathbf{D}_{a} \mathbf{V}_{\text{and}}, \tag{17}$$

where  $\Phi_n$  are the spatial modes,  $\mathbf{D}_a$  is the diagonal matrix of the amplitudes  $a_n$  of the DMD modes, and  $\mathbf{V}_{\rm and}$  is the Vandermonde matrix containing the eigenvalues  $\lambda_n$ , which determine the frequencies and decay rates of the modes. The amplitudes  $a_n$  are determined such that they optimally approximate the input data sequence. The reconstruction of the temporally developing data field is achieved by superposing the DMD modes. The DMD modes with the most relevant dynamic structures are determined using a sparsity-promoting algorithm by Jovanovic et al. [32]. For further details on the DMD algorithm, the reader is referred to Schmid [31] and Jovanovic et al. [32].

### 3. Numerical Burner Configurations

Next, the three burner configurations and the boundary conditions are described. In figure 1 a not-to-scale schematic of the geometry of the symmetric confined burner and its radial swirler<sup>1</sup> is shown. It corresponds to the experimental burner configuration by Moeck et al. [4]. The geometry includes the combustion chamber, the injector, a static radial swirler, and a part of the burner plenum. A fuel-lean mixture of methane and air with an equivalence ratio of  $\phi = 0.67$  enters the plenum.

Downstream of a converging nozzle, the radial swirler generates by its 9 blades an angular momentum. The resulting swirling jet has a swirl number, defined by the ratio of the axial fluxes of the azimuthal momentum and the

<sup>&</sup>lt;sup>1</sup>The detailed data of the geometry were provided by EM2C.

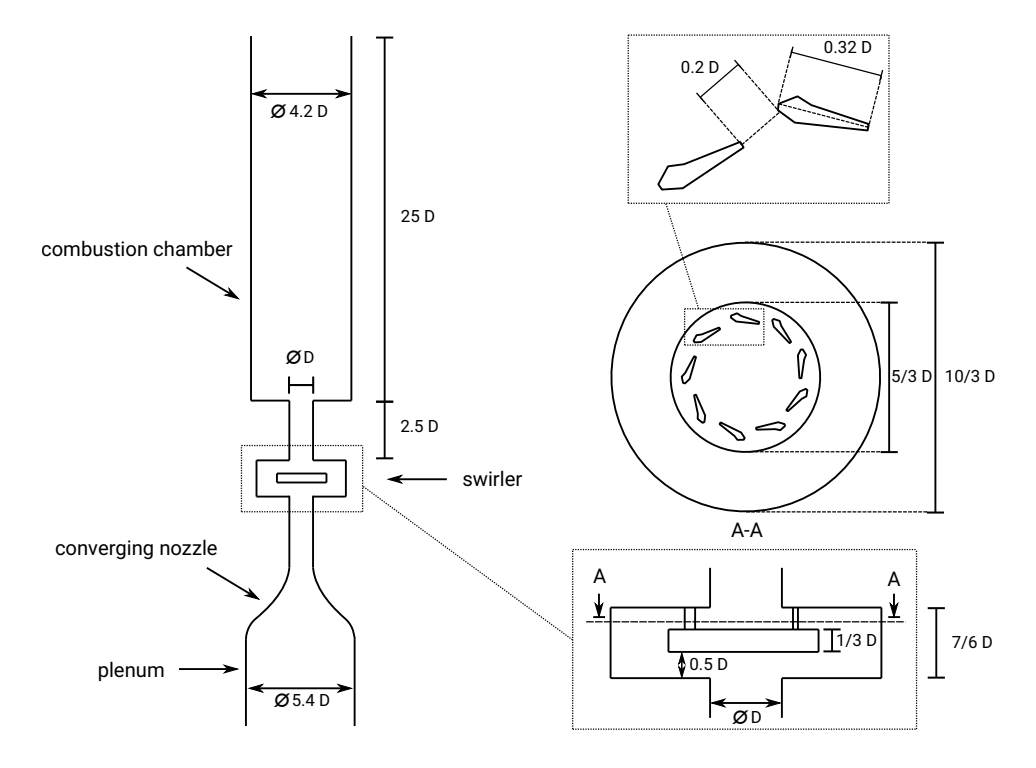


Figure 1: Not-to-scale schematic of the geometry of the burner (left) and the radial swirler (right). The size of the injection tube diameter is D = 12mm.

axial momentum [33]

$$S = \frac{\int_0^R \rho v_{ax} v_{\theta} 2\pi r^2 dr}{R \int_0^R \rho v_{ax}^2 2\pi r dr},$$
 (18)

of S=0.73, where r is the radial coordinate and R=D/2. The injector with a diameter of D=12mm has a length of 2.5D. The Reynolds number based on the injector diameter and the bulk velocity is Re=8,800. The combustion chamber is located downstream of the injector and has a length of 25D.

The variation of the combustion chamber leads to the three numerical configurations shown in figure 2. An overview of the three setups and their notations is shown in table 1. The first swirl flame (SF) configuration SF<sub>open</sub>

Notation	Setup Description	$\phi$	p''(Pa)	$f_{ m PVC}({ m Hz})$	$\mathrm{Re}_D$
$SF_{open}$	unconfined swirl flame	0.67	-	880	8,800
$SF_{sym}$	symmetric confined swirl flame	0.67	700	880	8,800
SF <sub>asym</sub>	non-symmetric confined swirl flame	0.67	350	920	8,800

Table 1: Swirl flame (SF) configurations; equivalence ratio  $\phi$ , root-mean square value of the limit-cycle pressure amplitude of the thermoacoustic instability p'', frequency of the precessing vortex core (PVC)  $f_{\text{PVC}}$ , and Reynolds number based on the injector diameter and the bulk velocity  $\text{Re}_D$ .

consists of the open burner, i.e., the flame is unconfined. The unconfined swirl flame is surrounded by burnt gas. Therefore, the burnt gas temperature of the unconfined swirl flame is not altered by its environment. As shown in figure 2(a), the computational domain downstream of the flame has an axial extent of 100D and a radial extent of 90D. Note that the boundary with normal parallel to the flow direction is formulated as a slip wall boundary. Due to the small axial velocity component near the location of this boundary the effect of this boundary formulation with respect to the qualitative analysis is expected to be negligible. Nevertheless, in future simulations a boundary formulation that takes into account the air entrainment of the unconfined flame will be imposed. The second configuration SF<sub>sym</sub> is shown in figure 2(b). It includes the combustion chamber with a diameter of approximately 4.2D which symmetrically confines the swirl flame. The third configuration SF<sub>asym</sub> includes the same combustion chamber which is, however, positioned non-symmetric to the flame. The distance between the centerline of the combustion chamber and the centerline of the injector exit is 0.7D as shown in figure 2(c). To ensure the correct acoustic impedance

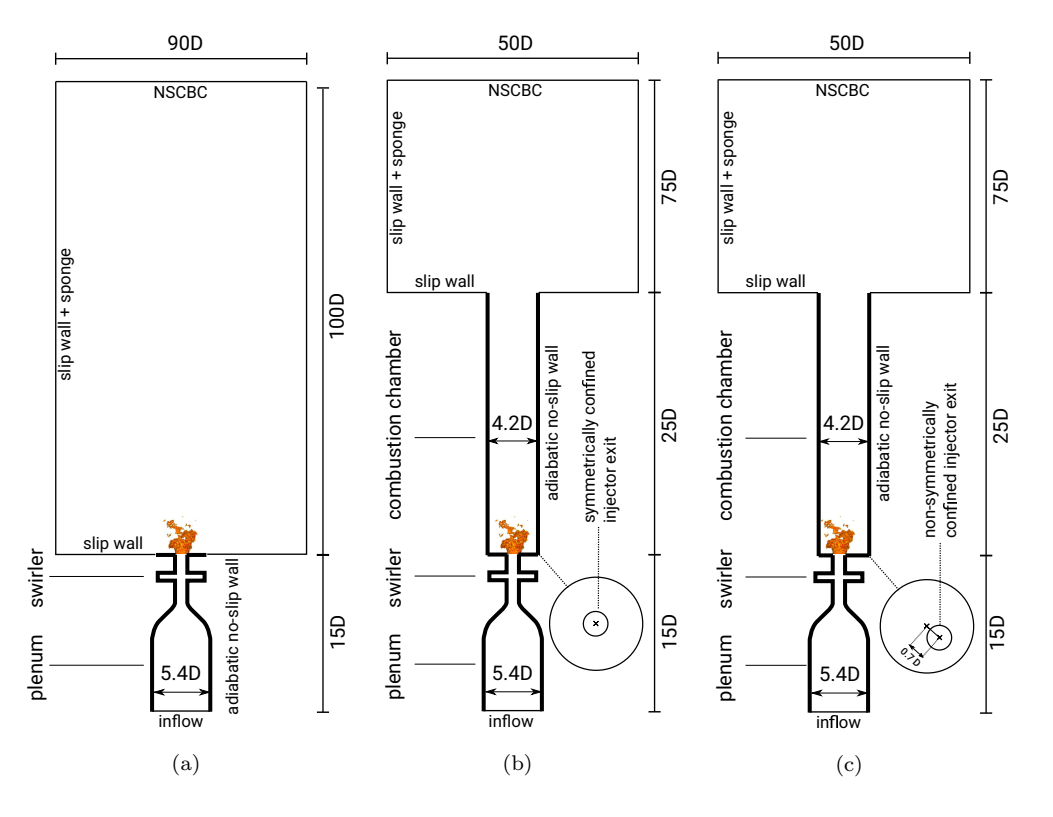


Figure 2: Not-to-scale schematic of the computational setups including boundary conditions; unconfined configuration ( $SF_{open}$ ) (a), symmetric confined configuration ( $SF_{sym}$ ) (b), and non-symmetric confined configuration ( $SF_{asym}$ ) (c).

downstream of the injector, the computational domain of the confined configurations is extended downstream of the combustion chamber by an additional volume.

In all three configurations adiabatic no-slip boundary conditions are imposed on the burner walls. Note that the wall temperature can have a significant impact on the combustion instabilities of swirl burners as shown, e.g., in Krause et al. [34]. This has to be taken into account when possible sources of discrepancies between the numerical and the experimental

results are discussed. The inflow and outflow boundary conditions are formulated as non-reflecting Navier-Stokes characteristic boundary conditions (NSCBC) [35], which reduce acoustic reflections at the boundaries. The NSCBC formulation defines a set of characteristic equations at the boundary. The wave amplitude variations of entering and exiting waves are determined by assuming locally one-dimensional inviscid relations. The exiting waves are determined from interior points of the computational domain using one-sided differences and the entering waves are set to zero. A linear relaxation coefficient as suggested by Rudy and Strikwerda [36] is used to avoid a drift of the imposed mean quantities. On the other boundaries, a slip wall boundary condition is applied and a pressure sponge layer [37] is used to dampen acoustic reflections at the sides of the outer domain.

The Cartesian mesh has the highest resolution in the region of the flame and the swirler geometry. A grid convergence study was performed in Herff et al. [12]. A cell spacing of  $\Delta x = 0.0115D = 0.138$ mm is required in this region to resolve the essential turbulent scales and to achieve a detailed agreement of the root-mean square profiles of the fluctuations of the axial and radial velocity components in the flame region with experimental measurements. This cell spacing corresponds to a resolution with respect to the laminar flame thickness  $l_F$  of approximately  $\frac{\Delta x}{l_F} = 0.34$ . For the finite-volume solver the chosen resolution leads to approximately  $200 \cdot 10^6$  cells for the confined configurations and  $350 \cdot 10^6$  cells for the unconfined configuration. Since the solution adaptive level-set solver has cells on the highest resolution only in the flame region, its mesh consists of fewer cells, i.e., there are approximately

# $7 \cdot 10^6$ cells. The supercomputing system "Hazel Hen" <sup>1</sup>

The numerical results in the following sections are obtained from snap-shots which were extracted at a frequency of 70 kHz for 16ms. Consequently, the results are accurate for frequencies greater than approximately 600Hz. Note that 10 cycles of the limit-cycle oscillations and 14 PVC cycles are included in the analyzed period.

#### 4. Results

The discussion of the results is structured as follows. First, the results of the SF<sub>sym</sub> configuration [12] are compared to experimental data [4] in section 4.1. The impact of confinement on the recirculation zones is discussed in section 4.2. Then, the effect of confinement on the precessing vortex core (PVC) and the movement of the flame due to the PVC is analyzed in sections 4.3 and 4.4. In section 4.5, the reduction of the limit-cycle amplitude of the thermoacoustic instability due to non-symmetric confinement will be shown. The first influencing factor to the reduced limit-cycle amplitude is discussed in section 4.6 where discrepancies in the distribution and intensity of the turbulent kinetic energy caused by the confinement are analyzed. Finally, the dominant dynamic modes of the three configurations are identified and analyzed in section 4.7 using a sparsity-promoting DMD algorithm

<sup>&</sup>lt;sup>1</sup>Details on the computing system are found at https://www.hlrs.de/systems/cray-xc40-hazel-hen/ was used for the simulations. The simulations of the confined configurations were performed using 6,000 cores and the simulation of the unconfined configuration was performed using 12,000 cores. The wall-time of both simulations was approximately 90 days leading to a total of  $50 \cdot 10^6$  CPU hours.

and another influencing factor to the reduced limit-cycle amplitude of the thermoacoustic instability is determined.

#### 4.1. Validation

Note that the following numerical-experimental comparison was already discussed in [12]. The essence of the presentation is summarized to make this manuscript self-consistent. The flow field statistics of the  $SF_{sym}$  configuration [12] is compared to measurement data by Moeck et al. [4]  $\frac{1}{6}D$ downstream of the injection tube in figure 3. It is evident that the mean axial and azimuthal velocity components and the corresponding RMS profiles are in good agreement. The axial velocity has the shape of an annular jet with a backflow on the centerline of the injector. The azimuthal mean velocity shows the rotational character of the jet with a velocity maximum of approximately 75% of the axial velocity component. The axial RMS profile evidences a maximum in the inner shear layer of the jet and a secondary peak in the outer shear layer. The azimuthal RMS profile has a maximum on the centerline and a maximum in the inner shear layer. The high values of the RMS profiles are not purely caused by turbulent fluctuations. It is primarily the coherent fluctuations from the precessing vortex core [38] that determine the velocity fluctuations. In the next sections, further comparisons between the numerical results with the measurements by Moeck et al. will be discussed. Note that the following results will further validate the computations. That is, a good agreement of the PVC frequency and the flame shape with the experimental results is evident and the qualitative comparison of the unconfined and confined configurations matches findings from the literature.

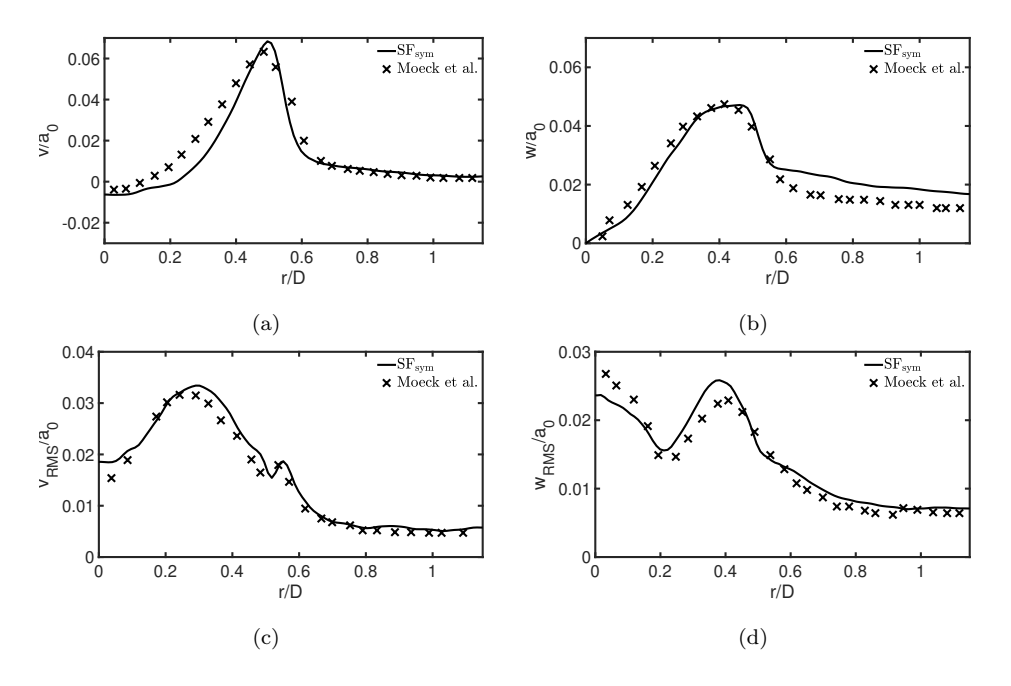


Figure 3: Radial distributions of the axial (left) and azimuthal (right) velocity components. Profiles of the mean components (top) and of the RMS values (bottom)  $\frac{1}{6}D$  downstream of the injection pipe; symbols are measurements by Moeck et al. [4] and the solid line denotes the numerical solution of the SF<sub>sym</sub> configuration [12].

## 4.2. Recirculation zones

The results in the following figures of this section are ordered such that first the unconfined  $SF_{open}$ , then the symmetric  $SF_{sym}$ , and finally the non-symmetric configuration  $SF_{asym}$  are addressed. To analyze the effect of confinement on the recirculation zones, the contours of the mean axial velocity component of the  $SF_{open}$  (a), the  $SF_{sym}$  (b), and the  $SF_{asym}$  (c) configurations are shown in figure 4. For all configurations an annular jet with an inner recirculation zone, i.e., a backflow region on the centerline, is present. However, the inner recirculation zone is clearly less extended in the  $SF_{open}$  configuration. Furthermore, the outer recirculation zones only occur in the

confined configurations. Due to the outer recirculation zone the spreading angle of the annular jet is higher for the confined configurations such that the jets are curved towards the burner walls. Similar results regarding the effect of confinement on the recirculation zones of symmetric confined and unconfined swirl flames were reported by Nogenmyr et al. [6]. The SF<sub>asym</sub> and SF<sub>sym</sub> configurations feature the same general structure of the mean axial flow field. However, in the SF<sub>sym</sub> configuration, the velocity field and the pressure field are symmetric. Due to the non-symmetric confinement the flow field changes significantly in the SF<sub>asym</sub> configuration. That is, the velocity magnitude is smaller in the region of the combustion chamber that is further away from the centerline of the injector. Consequently, the pressure in this region is increased. The resulting pressure field in the combustion chamber causes the gas from this region to flow towards the center which results in a smaller inner recirculation zone in the SF<sub>asym</sub> configuration.

## 4.3. Precessing vortex core

To determine the PVC frequency, spectra of the axial velocity component of the three configurations are shown in figure 5. The blue/red/black lines correspond to the  $SF_{open}/SF_{sym}/SF_{asym}$  configurations.

The spectra of the axial velocity component are determined from a probe located in the inner shear layer of the annular jets at  $(r, y) = (\frac{1}{3}D, \frac{1}{6}D)$ . Two peaks are evident in all spectra. The first peak at roughly 880Hz for all configurations corresponds to a counter-rotating single helix spiral breakdown, which is often referred to as the precessing vortex core. This frequency of the PVC is in good agreement with the frequency 880Hz found by Moeck et al. [4]. The second peak at approximately 1800Hz is caused by a second

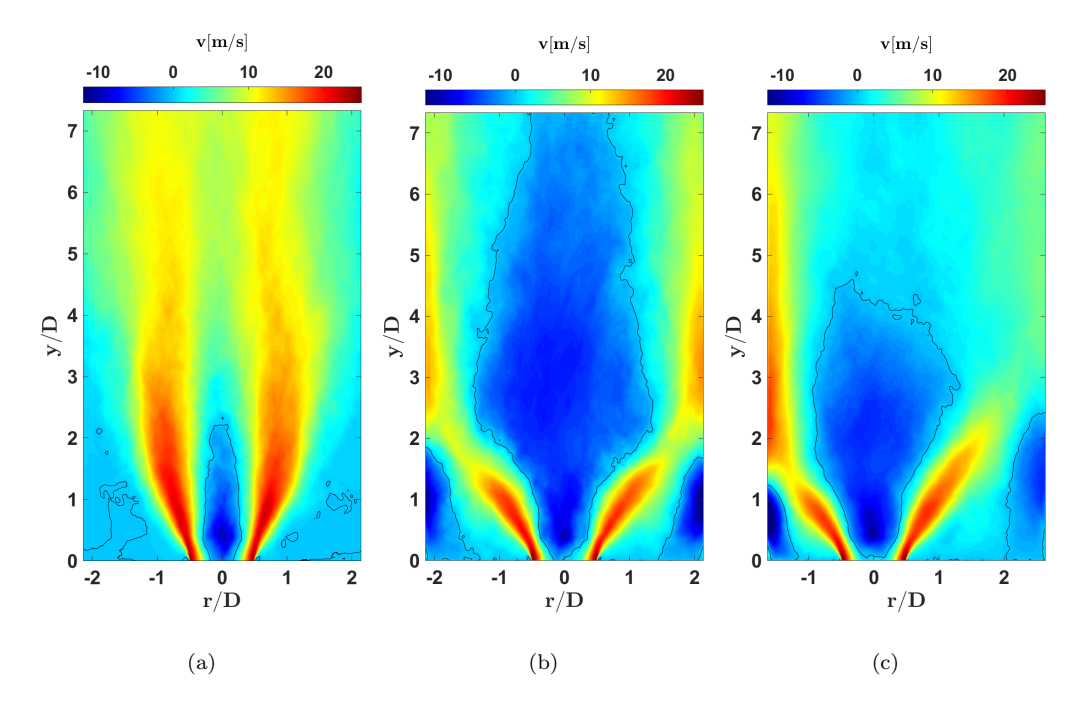


Figure 4: Contours of the mean axial velocity component. The solid black lines define zero contours of the axial velocity;  $SF_{open}$  (a),  $SF_{sym}$  (b) [12], and  $SF_{asym}$  (c).

vortex breakdown, which is a counter-rotating double helix spiral. Thus, two helical instability modes coexist for this swirl burner. Since the second helical mode hardly impacts the flame of the current burner configurations, it will not be analyzed any further. Note that the coexistence of two dominant helical instabilities in turbulent swirling flow configurations has been investigated in the literature, e.g., in Vanierschot et al. [39].

It has to be emphasized that the frequencies of both modes are identical for the  $SF_{open}$  and the  $SF_{sym}$  configurations, whereas the helical mode frequencies of the  $SF_{asym}$  configuration are slightly higher (table 1).

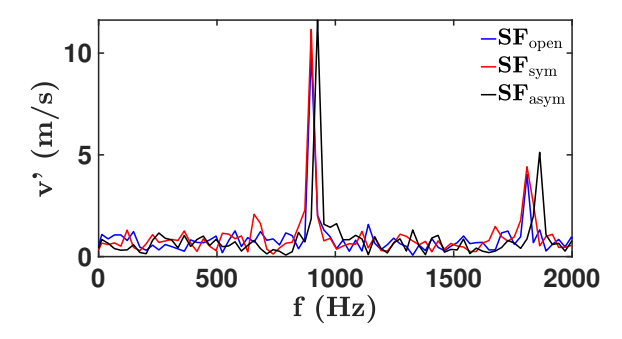


Figure 5: Spectra of the axial velocity component at  $(r, y) = (\frac{1}{3}D, \frac{1}{6}D)$ ; the blue/red/black lines denote the  $SF_{open}/SF_{sym}/SF_{asym}$  configurations.

## 4.4. Flame movement

To analyze the impact of confinement on the flame motion, the flame shapes of the numerical solutions are comparatively juxtaposed in figure 6. Additionally, the experimental data from Moeck et al. [4] are illustrated. The experimental images show a seeding of the unburnt gas and the images of the numerical results show the progress variable, i.e., a value of 0 corresponds to unburnt gas and a value of 1 corresponds to burnt gas. Therefore, the flame shapes can be directly compared. The images are phase averaged with respect to the frequency of the PVC at equidistant phase angles, i.e., from the left to the right at  $0^{\circ}$ ,  $120^{\circ}$ , and  $240^{\circ}$ . The results are arranged from top to bottom: experimental results by Moeck et al. [4], numerical results of the SF<sub>open</sub>, SF<sub>sym</sub> [12], and SF<sub>asym</sub> configurations.

The flame movement of the  $SF_{sym}$  configuration is in good agreement with the experimental results. That is, the flame foot is displaced by the PVC which yields a rotating flame in the combustion chamber, as reported by Moeck et al. [4]. The flame of the  $SF_{asym}$  configuration shows the same

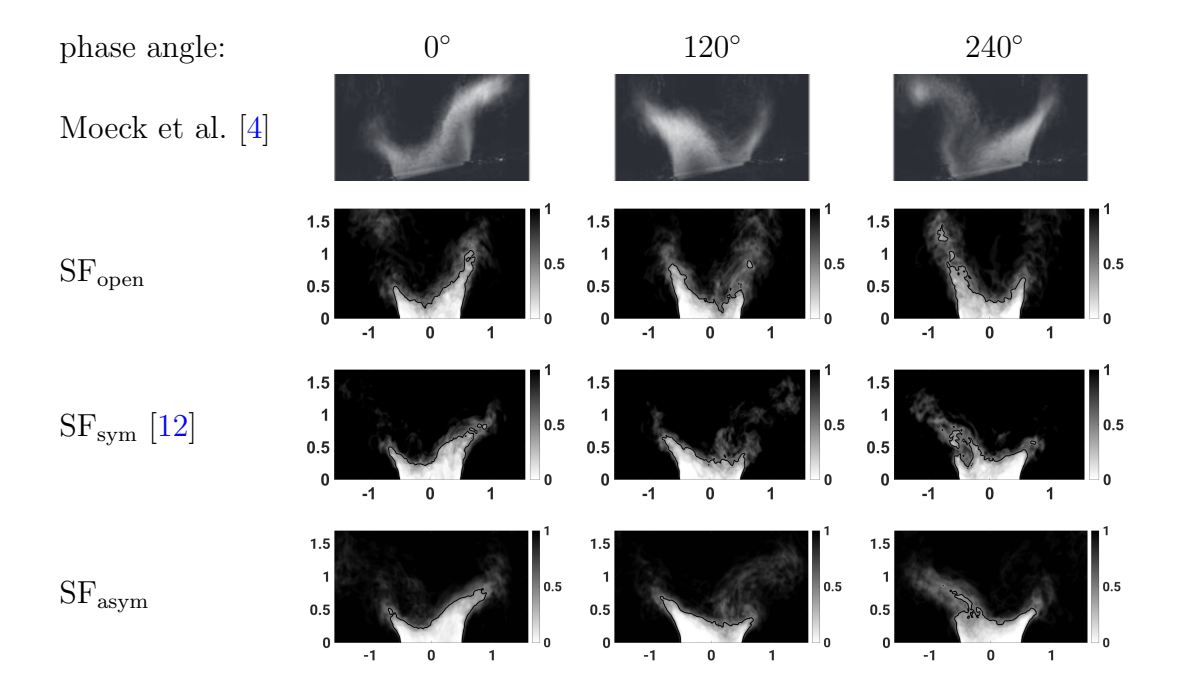


Figure 6: Phase averaged images of the flame with respect to the PVC frequency at equidistant phase angles, i.e., starting from the left at  $0^{\circ}$ ,  $120^{\circ}$ , and  $240^{\circ}$ . From top to bottom: Moeck et al. [4],  $SF_{open}$ ,  $SF_{sym}$  [12], and  $SF_{asym}$ .

movement, i.e., the non-symmetric confinement has a low impact on the dynamics of the flame due to the PVC. However, the movement of the  $SF_{open}$  configuration shows significant discrepancies. The shape of the flame of the  $SF_{open}$  configuration is less curved and the position of the axis of the flame foot is closer to the centerline of the injector. It will be shown in section 4.7 that the different behavior of the flame of the  $SF_{open}$  configuration is caused by the PVC desintegrating shortly downstream of the injector exit.

### 4.5. Thermoacoustic instability

The impact of non-symmetric confinement on the thermoacoustic instability is analyzed next. The spectra of the pressure downstream of the flame are shown in figure 7. They are determined 5D downstream of the injector. Note that the results are essentially independent of the exact location of the probe since the dominant peaks in the spectra are caused by a plain acoustic mode with a relatively large wave length. Evidently, an instability mode exists in the confined configurations at 660Hz. This frequency is higher than the frequency 540Hz found by Moeck et al. [4]. Moeck et al. [4] stated that the burnt gas temperature in their experiment is lower than the theoretical adiabatic burnt gas temperature due to heat loss at the wall. In the LES, the higher temperature leads to the higher speed of sound and to the increased quarter-wave frequency. The LES results match the theoretical frequency of

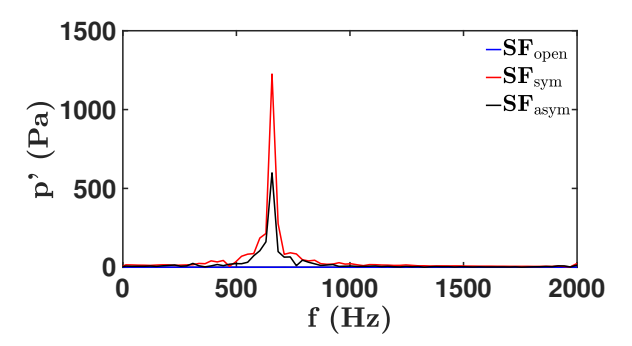


Figure 7: Spectra of the pressure 5D downstream of the injector; the blue/red/black lines denote the  ${\rm SF_{open}/SF_{sym}/SF_{asym}}$  configurations.

the quarter-wave resonance mode for a combustion chamber filled with burnt gas at the temperature of an adiabatic combustion process taking into account the end correction of the combustion chamber [4]. Since the instability is related to a resonance mode of the combustion chamber it is not observed in the unconfined configuration. Note that the amplitude of the limit-cycle instability differs for the two confined configurations. To be more precise, the limit-cycle amplitude of the  $SF_{asym}$  configuration is significantly reduced.

In figure 8, the spectra of the integrated heat release of the  $SF_{open}$ ,  $SF_{sym}$ , and  $SF_{asym}$  configurations are shown. The broadband spectra of all configurations are similar. However, the spectrum of the  $SF_{sym}$  configuration has a peak in the range of the frequency of the limit-cycle instability at 650Hz. This shows the coupling of the integrated heat release of the flame of the  $SF_{sym}$  configuration with the pressure fluctuations in the combustion chamber.

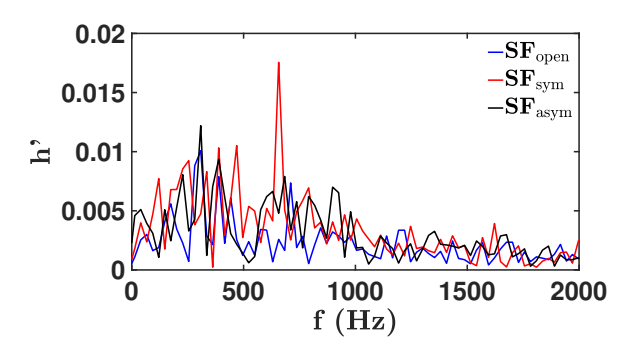


Figure 8: Spectra of the integrated heat release of the swirl flames; the blue/red/black lines denote the  $SF_{open}/SF_{sym}/SF_{asym}$  configurations.

The response of the integrated heat release of the SF<sub>asym</sub> configuration is significantly reduced. The non-symmetry possibly impacts the flame transfer function (FTF) such that the response of the flame to the acoustic excitation at the quarter-wave frequency is altered. It is known that the confinement, i.e., the ratio of confinement, can have a significant impact on the FTF [40]. However, to the best of the authors' knowledge the impact of non-symmetric

confinement on the FTF has not yet been thoroughly investigated. In section 4.7, another explanation for a lower coupling of the acoustic oscillations with the flame will be given.

#### 4.6. Turbulent kinetic energy distribution

In figure 9, the contours of the mean turbulent kinetic energy k are shown. In the  $SF_{sym}$  and  $SF_{asym}$  configurations, zones of high turbulence intensity are evident in the annular jets which are less pronounced in the  $SF_{open}$  configuration. The turbulence intensity is clearly increased by the confinement due to the stronger curvature of the flame. Furthermore, the velocity fluctuations are increased due to the outer recirculation zone in the confined configurations which interacts with the outer shear layer of the swirl jet due to the high radial velocity component of the flow constricting the jet. Similar results from experimental data regarding the effect of confinement on the turbulent kinetic energy of confined and unconfined swirl flames were reported by Khalilhasan et al. [7].

#### 4.7. Dynamic Mode Decomposition

To analyze the most important dynamic modes of the  $SF_{open}$ ,  $SF_{sym}$ , and  $SF_{asym}$  configurations, results of the sparsity-promoting DMD algorithm are discussed in the following.<sup>1</sup> All DMD results are obtained using N = 150

<sup>&</sup>lt;sup>1</sup>Note that a proper orthogonal decomposition (POD) analysis was performed. The identified POD modes corresponded to the following DMD modes. Since the POD modes can contain contributions from a broad temporal spectral information of the flow, the interpretation of the results can be misleading. The modes determined by the DMD algorithm correspond to specific frequencies. Therefore, the modal analysis focuses on the

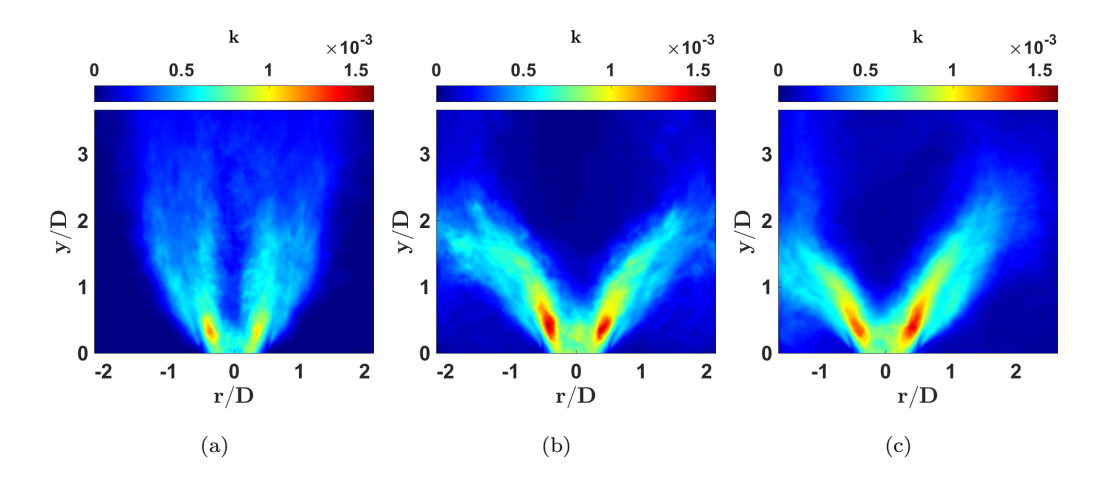


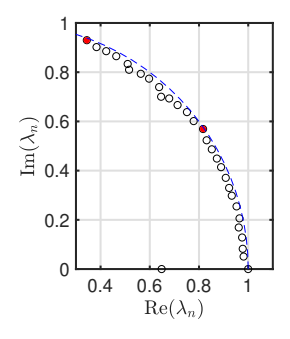
Figure 9: Contours of the mean turbulent kinetic energy k;  $SF_{open}$  (a),  $SF_{sym}$  (b), and  $SF_{asym}$  (c).

samples of the three-dimensional velocity field in the injection tube and up to 7D downstream of the injector. The samples are equidistantly distributed with a frequency of 9,500Hz. To reduce the computational cost of the DMD, the spatial resolution of each sample is reduced by using every second point of the LES results. To understand the details of the temporal dynamics of the modes, which are discussed in the following, it is really necessary to watch the videos of the DMD modes. These videos of all DMD modes are available in the supplementary material.

First, the  $SF_{open}$  configuration is considered. As discussed in section 4.3, two helical instabilities coexist in this burner configuration. Since the  $SF_{open}$  swirl flame is not confined, no interaction with the geometry downstream of the injector exists. Therefore, the DMD results are expected to identify these

DMD results.

two helical instability modes as the dynamically most crucial modes. The DMD spectrum of the  $SF_{open}$  configuration is shown in figure 10. The complex DMD eigenvalues  $\lambda_n$  are plotted together with the unit circle to assess the decay rates of the DMD modes. The amplitudes  $a_n$  of the DMD modes are normalized by the amplitude  $a_0$  of the mean mode and multiplied by their damping  $|\lambda_n|^N$ . The amplitudes of transient modes that immediately decay and consequently are of minor importance for the overall velocity field are reduced by the multiplication by the damping factor. The red markers denote the most crucial modes identified by the sparsity-promoting algorithm. As predicted the two most important modes are identified for the PVC fre-



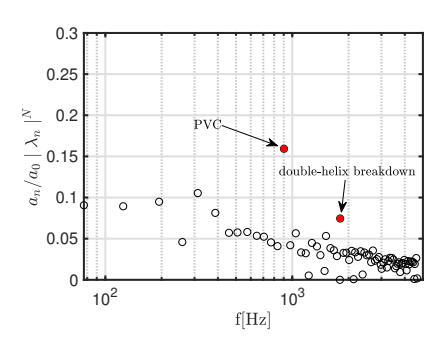


Figure 10: DMD eigenvalues (left) and normalized amplitudes (right) of the velocity fields of the  $SF_{\rm open}$  configuration. The red markers denote the most crucial DMD modes, which correspond to the PVC modes.

quency at approximately 900Hz and the second helical instability mode of the burner at approximately 1800Hz.

To visualize the three dimensional shape and the temporal evolution of the identified DMD modes, the modes are superimposed with the mean mode and reconstructed in time. The contour of a constant value of the Q-criterion of the resulting velocity field of the first DMD mode is shown in figure 11 to illustrate the structure of the PVC of the  $SF_{open}$  configuration. The images in figure 11 present the beginning of the DMD mode and the mode at half its period. The precessing vortex core is clearly visible in the injection tube

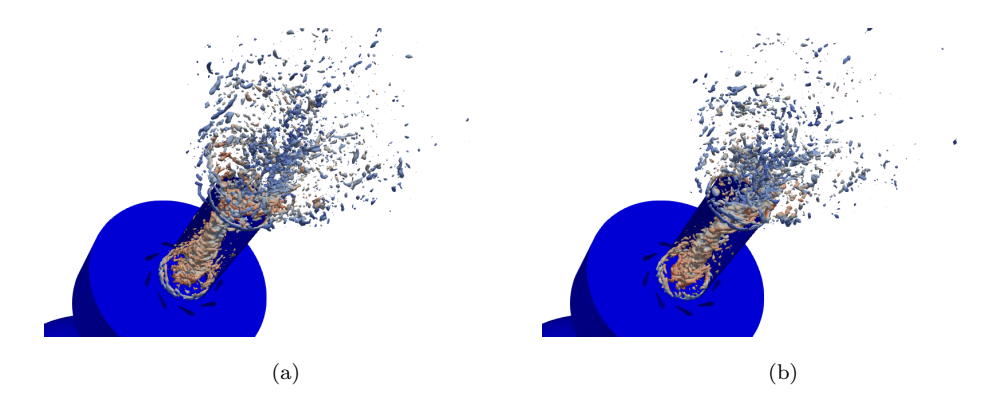


Figure 11: Contours of the Q-criterion of the reconstructed velocity field of the  $SF_{open}$  configuration using the mean mode and the PVC mode at the beginning of the DMD mode (a) and at half its period (b). Contours are colored by the velocity magnitude. A video of the DMD mode is available in the supplementary material. Watch the video to see the details of the dynamics of the mode.

of the burner. The PVC rotates at the injector exit and dissolves shortly downstream of the injector. It was discussed in section 4.4 that the less pronounced movement of the flame in figure 6 compared to the confined configurations is due to the desintegration of the PVC.

In figure 12, the eigenvalues and normalized amplitudes of the  $SF_{sym}$  (a) and  $SF_{asym}$  (b) configurations are shown. For both configurations, the most important dynamic mode is the PVC mode. A second stable DMD mode is only found for the  $SF_{sym}$  configuration. However, in contrast to the unconfined configuration the frequency of the second mode corresponds to the limit-cycle instability at approximately 660Hz. The DMD mode correspond-

ing to the same frequency for the  $SF_{asym}$  configuration is marked by the blue dot in figure 12(b).

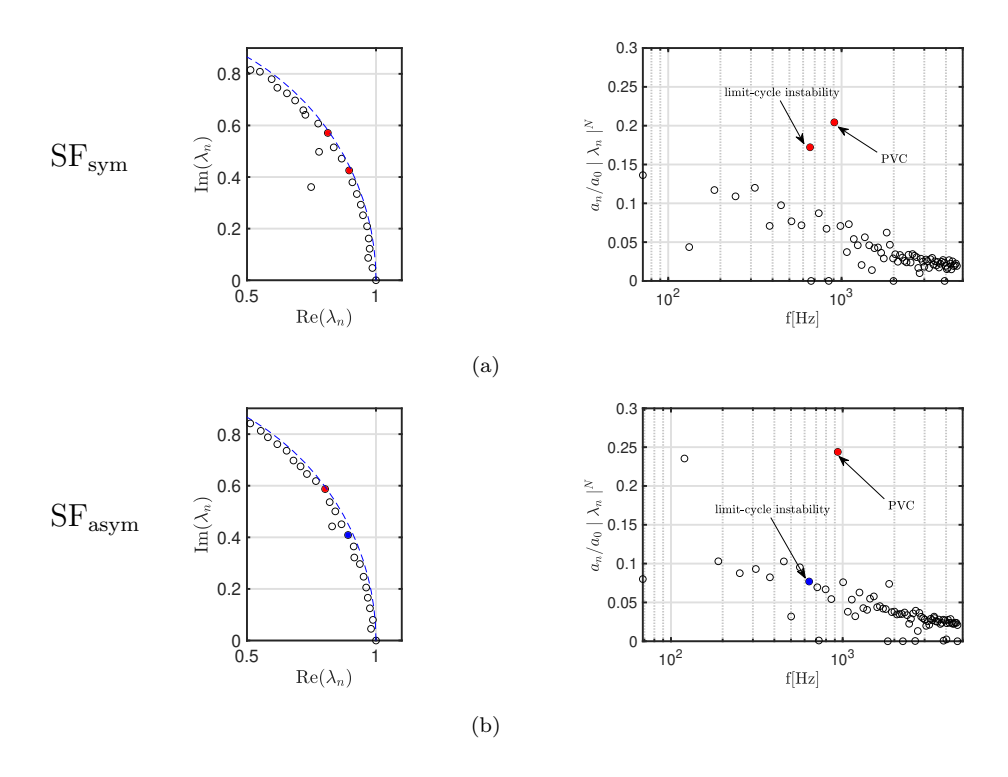


Figure 12: DMD eigenvalues (left) and normalized amplitudes (right) of the velocity fields the  $SF_{sym}$  configuration (a), and the  $SF_{asym}$  configuration (b). The red marker denote the most crucial DMD mode, which corresponds to the PVC mode. The blue marker in the results of the  $SF_{asym}$  configuration denotes the DMD mode corresponding to the frequency of the thermoacoustic instability.

Note that the eigenvalues of the two DMD modes are close to the unit circle in the  $SF_{sym}$  configuration, i.e., they are stable modes, whereas all other modes have a significant decay rate, i.e., they are transient modes. The limit-cycle instability mode of the  $SF_{asym}$  configuration shows a decay rate smaller than unity and is, therefore, no stable mode. Hence, it can be

stated that the interaction of the pressure fluctuations with the velocity field evidences a stable DMD mode at the corresponding frequency only for the  $SF_{\rm sym}$  configuration.

The temporal reconstruction of the PVC modes are shown for the  $SF_{sym}$  configuration in figures 13 (a) and (b) and for the  $SF_{asym}$  configuration in figures 13 (c) and (d). Unlike the PVC mode of the  $SF_{open}$  configuration, the

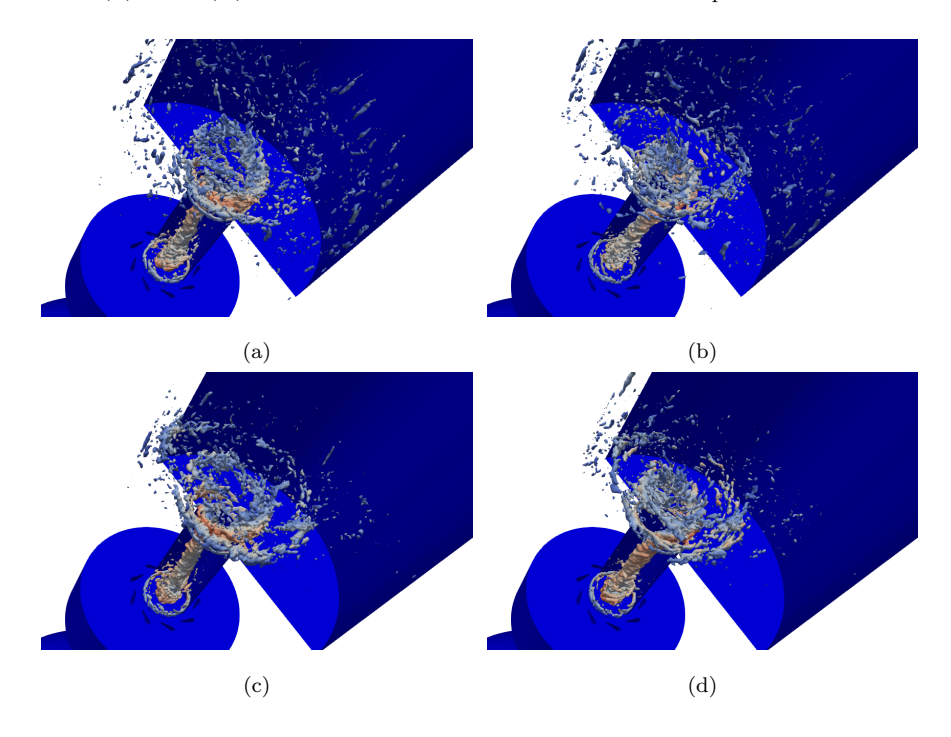


Figure 13: Contours of the Q-criterion of the reconstructed velocity field of the  $SF_{sym}$  configuration (a), (b) and the  $SF_{asym}$  configuration (c), (d) using the mean mode and the PVC mode at the beginning of the DMD modes (a), (c) and at half their period (b), (d). Contours are colored by the velocity magnitude. Videos of the DMD modes are available in the supplementary material. Watch the videos to see the details of the dynamics of the modes.

PVCs of the confined configurations do not immediately dissolve downstream

of the injector exit. The helical vortex core is a counter rotating spiral. Due to the confinement outer recirculation zones evolve and the inner recirculation zone increases significantly, which was discussed in section 4.2. Furthermore, the entire flow in the combustion chamber exhibits a considerable swirling motion. These changes to the flow field stabilize the PVC downstream of the injector which leads to the observed spiral structure. The structure of the PVC mode shows no significant differences due to the non-symmetric confinement, which is also evident from the phase averaged images of the flame shape in figure 6.

The temporal reconstruction of the second DMD mode, which is caused by the interaction of the velocity field with the acoustic pressure fluctuations of the limit-cycle instability, is shown in figure 14 for the SF<sub>sym</sub> configuration. Note that the reconstruction of this mode of the SF<sub>asym</sub> configuration reveals no clear structure in the velocity field, which is expected due to the significantly higher decay rate of the mode. Therefore, the DMD mode is shown only for the SF<sub>sym</sub> configuration. Evidently, the limit-cycle instability mode impacts the velocity field in two sections of the burner. In the injection tube, the mode describes a temporally periodic alternation of the PVC, i.e., the diameter of the core in the injection tube, the level of vorticity, and the level of the Q-criterion. Downstream of the injection tube a vortex ring forms in the flame region. To further evidence the vortex ring, in figure 15 the Q-criterion field (a) and the normal component of the vorticity field (b) of the reconstructed velocity field of the SF<sub>sym</sub> configuration are shown in a 2D plane just downstream of the injector. The black arrows indicate the direction of the reconstructed velocity vector. In figure 15(a), the core of

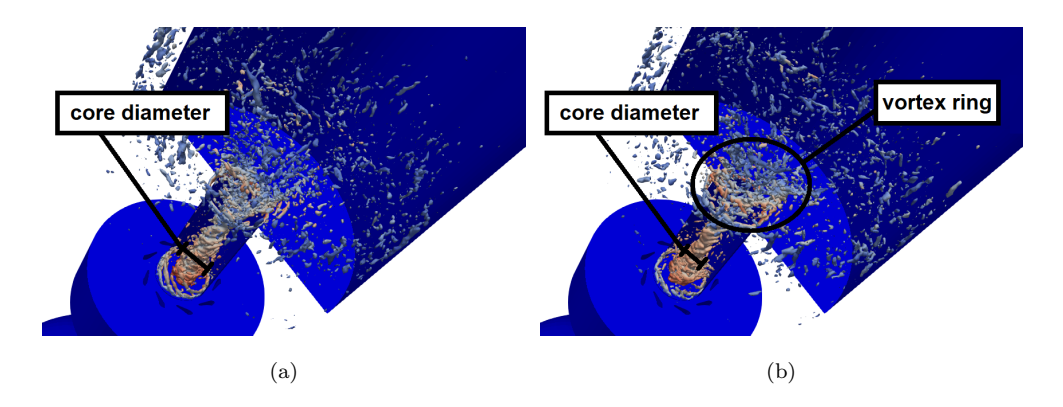


Figure 14: Contours of the Q-criterion of the reconstructed velocity field of the  $SF_{sym}$  configuration using the mean mode and the limit-cycle instability mode at the beginning of the DMD mode (a) and at half its period (b). Contours are colored by the velocity magnitude. A video of the DMD mode is available in the supplementary material. Watch the video to see the details of the dynamics of the mode.

the vortex ring is evident from the high values of the Q-criterion. Likewise, the high vorticity magnitudes in the same regions in figure 15(b) show the existence of the vortex ring. Furthermore, the direction of the velocity vector clearly indicates a vortex-like movement of the flow. This vortex ring arises close to the flame foot and propagates downstream over time. Note that a video of this illustration is available in the supplementary material in which the temporal evolution of the vortex ring becomes apparent. Since the vortex is in close vicinity to the flame, it is plausible that it causes fluctuations of the local heat release of the flame. Therefore, the second DMD mode emphasizes the coupling of the acoustic wave with the velocity field in the flame region. Consequently, the motion of the flame of the  $SF_{sym}$  is coupled with the acoustic wave which causes the high pressure amplitude of the limit-cycle instability, which was discussed in section 4.5.

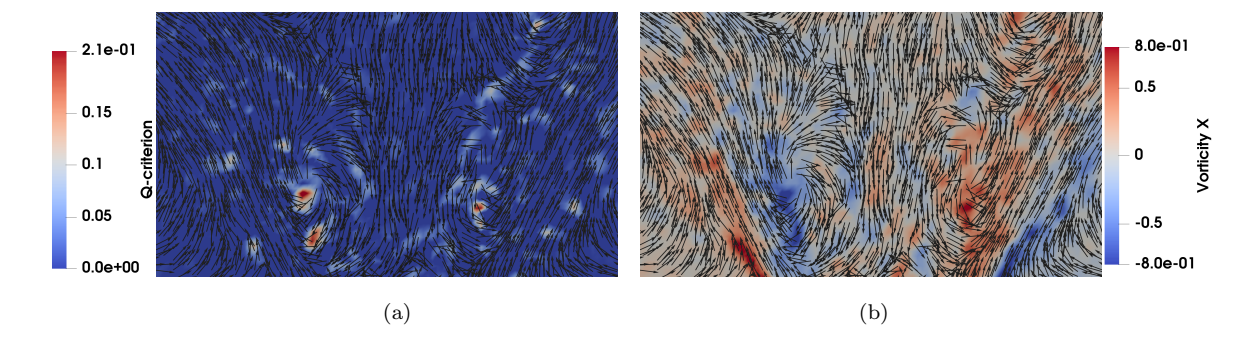


Figure 15: Contours of the Q-criterion (a) and the normal component of the vorticity (b) of the reconstructed velocity field of the  $SF_{\rm sym}$  configuration using the mean mode and the limit-cycle instability mode at half its period just downstream of the injector. The arrows indicate the direction of the reconstructed velocity vector. A video of this illustration is available in the supplementary material.

The non-existence of a stable vortex ring for the  $SF_{asym}$  configuration cannot be thoroughly explained. That is, it is unclear whether or not it is the non-symmetric flow field or the too low pressure amplitude of the limit-cycle instability. The former could explain a lower coupling of the acoustic wave of the limit-cycle instability with the flame and, consequently, the lower pressure amplitude of the limit-cycle instability due to the non-symmetric confinement.

## 5. Conclusions

The impact of confinement on a lean premixed turbulent swirl flame was investigated using large-eddy simulations. Three confinement approaches were considered, i.e., unconfined, symmetric confined, and non-symmetric confined configurations. Due to the large swirl number of the jet a precessing vortex core (PVC) occurred for this burner and due to the interaction of

the acoustic sources of the flame with the acoustic quarter-wave mode of the combustion chamber a thermoacoustic instability was present in the confined configurations. The results of the symmetric confined swirl flame could be compared to measurements by Moeck et al. and a good agreement with the data of the experiment was evident. That is, the profiles of the mean velocity components in the axial and azimuthal direction, the profiles of their rootmean square (RMS) values, the frequency of the PVC, and the motion of the flame at the PVC frequency were in good agreement. The frequency of the thermoacoustic instability was slightly increased compared to the experiment since the speed of sound in the numerical configurations was higher since heat losses at the walls of the combustion chamber were neglected.

The comparative juxtaposition of the confined configurations and the unconfined configuration confirmed various experimental findings from the journal literature. An outer recirculation zone existed near the combustion chamber walls only in the confined configurations and the turbulent kinetic energy (TKE) was higher compared to the unconfined swirl flame configuration. Furthermore, the inner recirculation zone was significantly smaller for the unconfined flame and the overall movement of the unconfined flame at the frequency of the PVC was less pronounced.

In both confined configurations a thermoacoustic instability was observed at the frequency of the acoustic quarter-wave mode of the combustion chamber. However, the limit-cycle amplitude of the instability was significantly reduced in the non-symmetric confined configuration. The broadband spectrum of the integrated heat release was similar for all three configurations. However, a peak due to a coupling with the acoustic oscillations at the thermoacoustic frequency occurred only in the symmetric confined configuration.

To analyze the dominant dynamic modes a sparsity-promoting dynamic mode decomposition (DMD) was performed using the velocity fields of the three configurations. In all three configurations, the most dominant dynamic mode was the PVC mode. The second most dominant mode was a second PVC mode in the unconfined configuration and in the symmetric confined configuration a mode at the frequency of the thermoacoustic instability. The temporal reconstruction of the PVC mode showed that the PVC of the unconfined configuration dissolved just downstream of the injection tube which explains the less pronounced movement of the unconfined swirl flame. Furthermore, the temporal reconstruction of the thermoacoustic instability mode of the confined configurations showed structures in the velocity field only for the symmetric confined configuration. In the symmetric confined configuration this mode describes the pulsation of the PVC diameter in the injection tube and a vortex ring forms downstream of the injection tube in the region of the flame. The vortex ring structure of this mode could not be determined for the non-symmetric confined configuration. This different flow structure is influenced by the lower limit-cycle amplitude of the thermoacoustic instability and the non-symmetric flow field.

To the best of the authors' knowledge this study is the first to investigate the effect of non-symmetric confinement on a single turbulent swirl flame. Note that a direct validation of the results of the non-symmetric confined configuration could not be presented since no experimental results of nonsymmetric confined flames are available in the literature. Despite the high quality of the used numerical methods, the authors would like to encourage experimental and numerical scientists to focus on the effect of non-symmetric confinement such that more validation data will be available in the future. The significant reduction of the limit-cycle amplitude of the thermoacoustic instability emphasizes that the results of symmetric confined swirl flames cannot directly be transferred to non-symmetric confined flames. That is, the position of swirl flames in the combustion chamber can have a significant impact on the stability of the burner facility.

### 6. Acknowledgments

This study was funded by the Deutsche Forschungsgemeinschaft (DFG, German Research Foundation) – GZ: SCHR 309/70-1, AOBJ: 639366. The authors are grateful for the computing resources provided by the High Performance Computing Center Stuttgart (HLRS) within a Large-Scale Project of the Gauss Center for Supercomputing (GCS).

## References

- T. Lieuwen, V. Yang, Combustion Instabilities in Gas Turbine Engines: Operational Experience, Fundamental Mechanisms, and Modeling. Progress in Aeronautics and Astronautics series, Vol. 210, AIAA, Reston, VA, 2005.
- [2] K. T. Kim, D. A. Santavicca, Interference mechanisms of acoustic/convective disturbances in a swirl-stabilized lean-premixed combustor, Combust. Flame 160 (2013) 1441–1457.

- [3] V. Caux-Brisebois, A. M. Steinberg, C. M. Arndt, W. Meier, Thermo-acoustic velocity coupling in a swirl stabilized gas turbine model combustor, Combust. Flame 161 (2014) 3166–3180.
- [4] J. P. Moeck, J.-F. Bourgouin, D. Durox, T. Schuller, S. Candel, Nonlinear interaction between a precessing vortex core and acoustic oscillations in a turbulent swirling flame, Combust. Flame 159 (2012) 2650–2668.
- [5] Y. M. Al-Abdeli, A. R. Masri, Review of laboratory swirl burners and experiments for model validation, Exp. Therm. Fluid Sci. 69 (2015) 178– 196.
- [6] K.-J. Nogenmyr, H. J. Cao, C. K. Chan, R. K. Cheng, Effects of confinement on premixed turbulent swirling flame using large eddy simulation, Combust. Theory Model. 17 (2013) 1003–1019.
- [7] A. E. E. Khalil, J. M. Brooks, A. K. Gupta, Impact of confinement on a swirl burner flowfield, AIAA Paper, 2017-1607 (2017).
- [8] A. J. De Rosa, S. J. Peluso, B. D. Quay, D. A. Santavicca, The effect of confinement on the structure and dynamic response of lean-premixed, swirl-stabilized flames, J. Eng. Gas Turbines Power 138 (2016) 061507.
- [9] L. Tay-Wo-Chong, W. Polifke, LES-based study of the influence of thermal boundary condition and combustor confinement on premixed flame transfer functions, Proc. ASME Volume 2: Combustion, Fuels and Emissions, Parts A and B (2012) 579–588.
- [10] G. Wang, X. Liu, L. Li, Z. X. Chen, F. Qi, Investigation on the flame

- front and flow field in acoustically excited swirling flames with and without confinement, Combust. Sci. Technol. (2019) 1–14.
- [11] D. Kim, J. Park, D. Han, K. T. Kim, Symmetry-breaking for the control of combustion instabilities of two interacting swirl-stabilized flames, Combust. Flame 194 (2018) 180–194.
- [12] S. Herff, A. Niemöller, M. Meinke, W. Schröder, LES of a turbulent swirl flame using a mesh adaptive level-set method with dynamic load balancing, Comput. Fluids 221 (2021) 104900.
- [13] K. Pausch, S. Herff, W. Schröder, Noise sources of an unconfined and a confined swirl burner, J. Sound. Vib. 475 (2020) 115293.
- [14] D. Hartmann, M. Meinke, W. Schröder, The constrained reinitialization equation for level set methods, J. Comput. Phys. 229 (2010) 1514–1535.
- [15] D. Hartmann, M. Meinke, W. Schröder, A level-set based adaptive-grid method for premixed combustion, Combust. Flame 158 (2011) 1318– 1339.
- [16] V. Moureau, B. Fiorina, H. Pitsch, A level set formulation for premixed combustion LES considering the turbulent flame structure, Combust. Flame 156 (2009) 801–812.
- [17] M. Meinke, W. Schröder, E. Krause, T. Rister, A comparison of secondand sixth-order methods for large-eddy simulations, Comput. Fluids 31 (2002) 695–718.

- [18] K. Pausch, S. Schlimpert, S. R. Koh, J. Grimmen, W. Schröder, The effect of flame thickening on the acoustic emission in turbulent combustion, AIAA Paper, 2016-2745 (2016).
- [19] S. Schlimpert, A. Feldhusen, J. H. Grimmen, B. Roidl, M. Meinke, W. Schröder, Hydrodynamic instability and shear layer effects in turbulent premixed combustion, Phys. Fluids 28 (2016) 017104.
- [20] H. Pitsch, A consistent level set formulation for large-eddy simulation of premixed turbulent combustion, Combust. Flame 143 (2005) 587–598.
- [21] U. Schumann, Subgrid scale model for finite difference simulations of turbulent flows in plane channels and annuli, J. Comput. Phys. 18 (1975) 376–404.
- [22] O. Colin, F. Ducros, D. Veynante, T. Poinsot, A thickened flame model for large eddy simulations of turbulent premixed combustion, Phys. Fluids 12 (2000) 1843–1863.
- [23] S. Schlimpert, S. Hemchandra, M. Meinke, W. Schröder, Hydrodynamic instability and shear layer effect on the response of an acoustically excited laminar premixed flame, Combust. Flame 162 (2015) 345–367.
- [24] K. Pausch, S. Herff, F. Zhang, H. Bockhorn, W. Schröder, Noise sources of lean premixed flames, Flow Turbul. Combust. 103 (2019) 773–796.
- [25] J. Boris, F. Grinstein, E. Oran, R. Kolbe, New insights into large eddy simulation, Fluid Dyn. Res. 10 (1992) 199–228.

- [26] C.-W. Shu, S. Osher, efficient implementation of essentially non-oscillatory shock capturing schemes, J. Comput. Phys. 77 (1988) 439–471.
- [27] L. Schneiders, C. Günther, M. Meinke, W. Schröder, An efficient conservative cut-cell method for rigid bodies interacting with viscous compressible flows, J. Comput. Phys. 311 (2016) 62–68.
- [28] T. Schilden, A. Pogorelov, S. Herff, W. Schröder, Microroughnessinduced disturbances in supersonic blunt body flow, Phys. Rev. Fluids 5, (2020) 063903 (2020).
- [29] R. Nourgaliev, T. Theofanous, High-fidelity interface tracking in compressible flows: Unlimited anchored adaptive level set, J. Comput. Phys. 224 (2007) 836–866.
- [30] S. Herff, K. Pausch, S. Schlimpert, H. Nawroth, C. Paschereit, W. Schröder, Impact of burner plenum acoustics on the sound emission of a turbulent lean premixed open flame, Int. J. Spray Combust. 12 (2020) 1–20.
- [31] P. J. Schmid, Dynamic mode decomposition of numerical and experimental data, J. Fluid Mech. (2010) 5–28.
- [32] M. R. Jovanovic, P. J. Schmid, J. W. Nichols, Sparsity-promoting dynamic mode decomposition, Phys. Fluids 26 (2014) 024103.
- [33] A. Gupta, D. Lilley, N. Syred, Swirl Flows, Abacus Press, Tunbridge Wells, England, 1984.

- [34] C. Krause, S. Laurent, P. Thierry, C. M. Arndt, H. Bockhorn, Influence of heat transfer and material temperature on combustion instabilities in a swirl burner, J. Eng. Gas Turbines Power 139, (2017) 051503 (2017).
- [35] T. Poinsot, S. K. Lelef, Boundary conditions for direct simulations of compressible viscous flows, J. Comput. Phys. 101 (1992) 104–129.
- [36] D. H. Rudy, J. C. Strikwerda, A nonreflecting outflow boundary condition for subsonic navier-stokes calculations, J. Comput. Phys. 36 (1980) 55–70.
- [37] J. B. Freund, Proposed inflow/outflow boundary condition for direct computation of aerodynamic sound, AIAA J. 35 (1997) 740–742.
- [38] M. V. Heitor, J. H. Whitelaw, Velocity, temperature, and species characteristics of the flow in a gas-turbine combustor, Combust. Flame 64 (1986) 1–32.
- [39] M. Vanierschot, J. Müller, M. Sieber, M. Percin, B. Van Oudheusden, K. Oberleithner, Single- and double-helix vortex breakdown as two dominant global modes in turbulent swirling jet flow, J. Fluid Mech. 883, (2020) A31 (2020).
- [40] A. Cuquel, D. Durox, T. Schuller, Scaling the flame transfer function of confined premixed conical flames, Proc. Combust. Inst 34 (2013) 1007– 1014.